



Research paper

Hollowed structured PtNi bifunctional electrocatalyst with record low total overpotential for oxygen reduction and oxygen evolution reactions



Gui-Rong Zhang*, Sebastian Wöllner

Ernst-Berl-Institut für Technische und Makromolekulare Chemie, Technische Universität, Darmstadt, 64287 Darmstadt, Germany

ARTICLE INFO

Keywords:
 PtNi bimetallic nanostructure
 Bifunctional electrocatalyst
 Total overpotential
 Oxygen evolution
 Oxygen reduction

ABSTRACT

Oxygen electrocatalysis plays a critical role in numerous energy storage/conversion devices, but the sluggish kinetics of both oxygen reduction reaction (ORR) and oxygen evolution reaction (OER) has greatly restricted the broad-based applications of such devices, especially for those requiring bifunctional electrocatalysts towards both reactions (e.g., regenerative fuel cells, metal-air batteries). Herein, we demonstrate that hollow structured bimetallic PtNi/C synthesized through a facile solution-based approach can be employed as a highly active bifunctional electrocatalyst for both ORR and OER, showing a combined ORR and OER overpotential of 0.69 V, which represents a record low value for a bifunctional electrocatalyst. Rotating ring disk electrode (RRDE) technique discloses that ORR was proceeding predominantly through the desired 4-electron pathway on the PtNi/C catalyst. Moreover, the PtNi/C is also found rather stable for both ORR and OER, with small activity lost after the accelerated durability test. These data echo the importance of innovative bi-/multi-metallic nanostructures for highly efficient catalysts that depend critically on using precious metals, for application in energy storage/conversion technologies.

1. Introduction

Electrochemical devices as unitized regenerative fuel cells (URFCs), and rechargeable metal-air batteries, which enable the facile interconversion between chemical and electrical energy, are considered as ideal solutions for the renewable energy storage/conversion [1–4]. One of the key challenges in commercialization of such devices is to search for highly efficient bifunctional electrocatalysts with low overpotential for both oxygen reduction reaction (ORR) and oxygen evolution reaction (OER), because of their slow reaction kinetics while different requirements on the nature of active sites for these two reactions [5–10]. Pt-based electrocatalysts are well known for their excellent activity for ORR but exhibit rather poor performance for OER, while in contrast, IrO_2 and RuO_2 are active catalysts for OER but barely active for ORR [11]. The state-of-the-art approach to a bifunctional electrocatalyst is to use Pt and $\text{IrO}_2/\text{RuO}_2$ in physical mixture or double-layer form, while the electrocatalytic performance of the mixed catalysts is usually compromised in presence of the second component [12–14]. Composite electrocatalysts prepared by alloying Pt with Ir or Ru have also been investigated as the bifunctional catalysts, but only moderate ORR and OER activities can be achieved [15–17]. High loadings of the noble metal electrocatalyst are thus needed to compensate the activity loss by using these mixed/composite electrocatalysts and also to overcome the

sluggish reaction kinetics of both ORR and OER [12,18], while the resulting high cost have greatly hindered the broad based application of the URFC and rechargeable metal-air batteries technology. Efforts were also made to develop non-precious-metal catalysts (NPMCs, e.g., metal oxides, perovskites oxides, carbon-based materials) as a bifunctional electrocatalyst [2,11,19], however, the synthesis of NPMCs usually involves tedious procedures and/or high temperature treatment, while satisfactory activity/stability can still be hardly achieved. Therefore, it remains a challenge to integrate efficient ORR and OER bifunctionality into one single catalyst.

PtNi nanoparticles represent one of the most active electrocatalysts for ORR [20,21], while it is also well documented that Ni-containing materials (e.g., oxides, (oxy)hydroxide) can exhibit excellent performance for OER [22–24]. Therefore, it can be expected that a proper combination of Pt with Ni could have great potential to give birth to efficient bifunctional electrocatalysts for both ORR and OER. Herein, as a proof-of-concept, we investigated carbon supported PtNi hollow nanoparticles with opened porous structure (PtNi/C) as a bifunctional electrocatalyst for ORR and OER in alkaline electrolyte. It turns out that the PtNi/C exhibits 3 times higher specific activity for ORR relative to the reference Pt/C. Moreover, PtNi/C is also found to be highly active and stable for OER, achieving a current density of 10 mA cm^{-2} at an overpotential of 350 mV, which even outperforms the benchmark IrO_2

* Corresponding author.

E-mail address: guirong.zhang@tc1.tu-darmstadt.de (G.-R. Zhang).

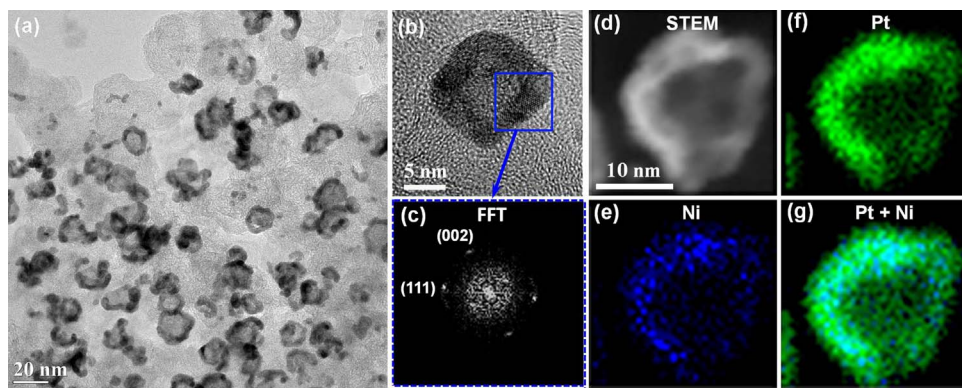


Fig. 1. Representative TEM (a), HRTEM/FFT (b, c), STEM (d) and EDS elemental mapping images (f-g) of PtNi/C sample.

C catalysts. The total overpotential, which is defined as the gap between the ORR half wave potential and OER overpotential at 10 mA cm^{-2} [5,6], is around 0.69 V on the PtNi/C, which represents the record low value to date for a bifunctional electrocatalyst. These data demonstrate the great promises of the PtNi/C as a new benchmark bifunctional electrocatalyst to be used in practical applications of URFC and/or rechargeable metal-air battery technologies.

2. Experimental

2.1. Synthesis of PtNi/C catalysts

The carbon supported PtNi hollow structured nanoparticles was synthesized by modifying a literature protocol [21]. Briefly, 137 mg of $\text{NiCl}_2 \cdot 6\text{H}_2\text{O}$, 176 mg of $\text{Pt}(\text{NH}_3)_4\text{Cl}_2 \cdot \text{H}_2\text{O}$ and 300 mg of carbon support (Ketjenblack EC300J, AkzoNobel) was firstly dispersed in 150 mL of deionized water-ethanol mixed solution (14:1, v/v) under vigorous stirring. After 30 min ultrasonic treatment of this mixture, a freshly prepared 1 mL of NaBH_4 (0.22 M) solution was added at a rate of 5 mL/min by using a syringe pump. After stirring the mixture for 1 h at room temperature, the solid sample was collected by filtration, intensively washed with deionized water and vacuum-dried at 80 °C overnight. The reference Pt/C and Ni/C catalysts were prepared by using the same procedure but without adding Ni or Pt precursor. The PtNi/C sample was further subject to acid treatment in 1 M H_2SO_4 for 22 h (R.T.) before electrochemical measurements.

2.2. Structural analysis

(Scanning) Transmission electron microscopy (STEM) analysis was performed on JEM-2100F (JEOL) operating at 200 kV. Energy dispersive spectroscopic (EDS) elemental mapping measurements were carried out in STEM mode with an X-ray detector (X-max80, Oxford Instruments). X-ray diffraction (XRD) was conducted in transmission geometry on an X-ray powder diffractometer (StadiP, Stoe & Cie GmbH) using $\text{Cu K}\alpha 1$ radiation ($\lambda = 1.540598 \text{ \AA}$) and Ge[111] monochromator. The porous property analysis was performed on a Quantachrome NOVA gas sorption analyzer using N_2 -sorption. The surface area was calculated by using the Brunauer-Emmett-Teller (BET) equation. ICP analyses were carried out at the Institute of Inorganic Chemistry and Analytical Chemistry (Johannes Gutenberg-University, Mainz, Germany). X-ray photoelectron spectroscopy (XPS) measurements were carried out on a SSX 100 ESCA Spectrometer using monochromatic $\text{Al K}\alpha$ radiation, and the binding energies were calibrated using the adventitious C 1s line at 284.8 eV. Spectra were evaluated using CasaXPS software with the Shirley type background.

2.3. Electrochemical measurements

Electrochemical measurements were conducted on a PARSTAT 4000

Potentiostat/Galvanostat controlled by a Versastudio software (AMETEK). A Hg/HgO electrode and Pt wire were used as reference and counter electrodes respectively. All potentials reported here in this work were calibrated against the reversible hydrogen electrode (RHE). A glassy carbon rotating disk electrode (RDE, $d = 5 \text{ mm}$, PINE) was used as the working electrode. Prior to use, the RDE was polished to a mirror finish using $0.05 \mu\text{m}$ γ -alumina suspension (Buehler), followed by ultrasonic cleaning with ethanol, acetone and deionized water to remove any contaminants. To prepare the working electrode, a catalyst suspension was firstly prepared by dispersing the catalyst powder in a mixed solvent of deionized water, isopropanol, and Nafion solution with the volume ratio of 4:1:0.025. Then $10 \mu\text{L}$ of the catalyst suspension ($2 \mu\text{g}/\mu\text{L}$) was deposited onto RDE. The electrochemistry measurements were carried out at room temperature in N_2 or O_2 saturated 0.1 M KOH electrolyte. Prior to the ORR and OER measurements, the electrolyte was purged with high purity O_2 for at least 30 min, followed by repeated cyclic voltammetry pretreatment (100 mV/s) of the electrocatalyst for up to 20 cycles until a stable voltammetry curve can be obtained. The ORR and OER performance was then evaluated by recording the ORR and OER linear scan voltammetry (LSV) curve at a scan rate of 10 mV/s and RDE rotation rate of 1600 rpm for each sample. Before determining the electrochemically active surface area (ECSA), the electrolyte was saturated with high purity N_2 for 30 min. The ECSA value of Pt was evaluated by measuring the charges associated with the reductive adsorption of protons on Pt surfaces, as detailed in the Supporting Information. The iR-drop effect was compensated for all the measurements, and the solution resistance was determined by conducting AC impedance analysis (10 kHz, 5 mV).

3. Results and discussion

3.1. Structural and morphological characterization

To probe the morphology and structure of the as-synthesized PtNi/C sample, TEM and EDS elemental mapping analyses were carried out. As shown in Fig. 1, the majority of the particles featured an irregular shape with an average diameter of 15.0 nm. The brighter contrast in the center evidenced the formation of the hollow structure of these PtNi nanoparticles. The HRTEM in combination with fast Fourier-transform (FFT) analyses revealed that the shell is comprised of crystalline structures with lattice spacings of 0.221 and 0.231 nm which are in agreement with (002) and (111) planes in a fcc PtNi phase, respectively. Fig. 1d–e display the STEM-EDS elemental mapping for a typical PtNi hollow nanoparticle, showing that Pt and Ni are homogeneously distributed within the shell while the outermost surface is enriched in Pt as a result of the acid leaching treatment. Moreover, the EDS elemental analysis indicates that the atomic Pt:Ni:C ratio is around 4.38: 0.44: 100, as shown in Fig. S1 of the Supporting Information. Although this value deviates from the ICP analysis result which gives an atomic Pt:Ni:C ratio of 1.86: 0.45: 100.00 (Table S1) probably due to the semi-

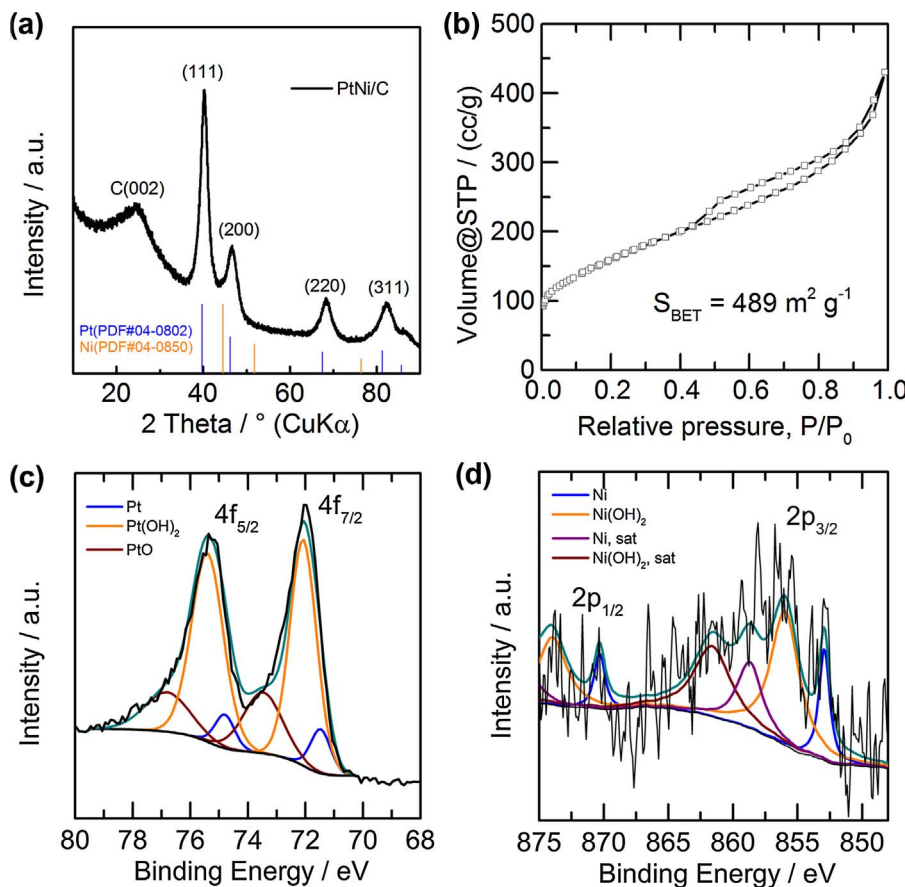


Fig. 2. XRD pattern (a), and N₂-sorption isotherm (b) of the hollow structured PtNi/C. Pt 4f (c) and Ni 2p (d) XPS spectra of the hollow structured PtNi/C.

quantitative nature of EDS technique, we can still learn that the majority of Ni species has been removed after the acid leaching treatment. The spontaneous formation of this unique hollow structure can be rationalized by the mechanism recently proposed by Chattot et al. based on comprehensive structural analyses of the intermediate particles formed at different growth stages [25]. Their work revealed that Ni species can be reduced first, and the pre-formed Ni particles will be embedded by a Ni_xB_yO_z shell due to the reaction between Ni²⁺ and oxidation products of NaBH₄; followed by a combined effect of the galvanic displacement process and the nanoscale Kirkendall effect which lead to the formation of Ni@Pt and ultimately the hollow structured PtNi nanoparticle [25].

The crystalline structure of the PtNi/C was further characterized by using XRD (Fig. 2a). Firstly, it can be seen that all the diffraction peaks shifted towards larger angles relative to those of the reference Pt, indicating a contracted Pt lattice distance. The average crystallite size and lattice parameter for PtNi/C were evaluated using the X-ray diffraction line width broadening method, and the results are summarized in Table S2. It can be seen that the crystallite sizes calculated with different diffraction peaks ((111), (200), (220), (311) and (222)) are in a comparable range, while later on the Pt (220) peak was selected for discussion to avoid the disturbance from the carbon support which presents no diffraction peak at around 68° [26]. It turns out that the Pt lattice has contracted by 1.3% relative to pure Pt (1.369 vs. 1.387 Å) due to the alloying with Ni [27], and the crystallite size is around 3.1 nm (detailed in the Supporting Information), which is comparable to the thickness of the PtNi shell (Fig. 1b). The texture properties of PtNi/C were characterized by using N₂-sorption (Fig. 2b), and the hysteresis between adsorption and desorption isotherm indicates the mesoporous nature of the sample with a BET surface area of 489 m² g⁻¹ and a total DFT pore volume of 0.52 cm³ g⁻¹. The surface composition and electronic state of PtNi/C sample was also studied using XPS.

Fig. 2c and d show the XPS signals for Pt 4f and Ni 2p. It can be found that both surface Pt and Ni are susceptible to be oxidized during the air exposure, as the XPS spectra of PtNi/C show that the majority of the surface Pt and Ni are in an oxidation state. However, in XRD studies, we can hardly identify any oxide or hydroxide species, which indicates that the surface oxide/hydroxide layers are likely in an amorphous structure while the bulk materials still tend to exist in a metallic state. Attempts were also made to calculate the surface Ni/Pt ratio for the as-prepared PtNi/C sample based on the XPS analysis, and interestingly we found that the surface Ni/Pt ratio of 0.25 is indeed quite comparable to the result given by ICP analysis (0.24). These results imply that the Ni species would distribute homogeneously all over the PtNi hollow particles. Although the surface is mainly composed of Pt, a small portion of Ni would also exist at the surfaces or subsurface regions even after the acid leaching treatment.

The surface redox properties of both Pt/C and PtNi/C catalysts were probed using cyclic voltammetry (CV) technique (Fig. S2). Firstly, it can be found that both catalysts show characteristic features of hydrogen adsorption/desorption on Pt in the low potential region, which can be utilized to estimate the ECSA of Pt [28], and the formation of the surface oxidation layer on Pt and the corresponding reduction process in the relatively high potential region (Fig. S2a) [29,30]. The ECSA of Pt/C and PtNi/C were determined to be 57.4 and 38.4 m² g_{Pt}⁻¹, respectively. It can be seen that the ECSA of PtNi/C is significantly lower than that of the reference Pt/C, which might arise from the relatively large particle size (15.0 nm) and shell thickness (3.5 nm). By adapting the method proposed by Dubau et al. in calculating the theoretical ECSA for a hollow structure particle [21], we estimated the theoretical ECSA of Pt based on a hollow structured particle model with similar particle diameter and shell thickness (detailed in the Supporting Information). It turns out that the inner surface area and outer surface area of this hollow particle model are 4.6 and 21.2 m² g_{Pt}⁻¹, respectively, giving a

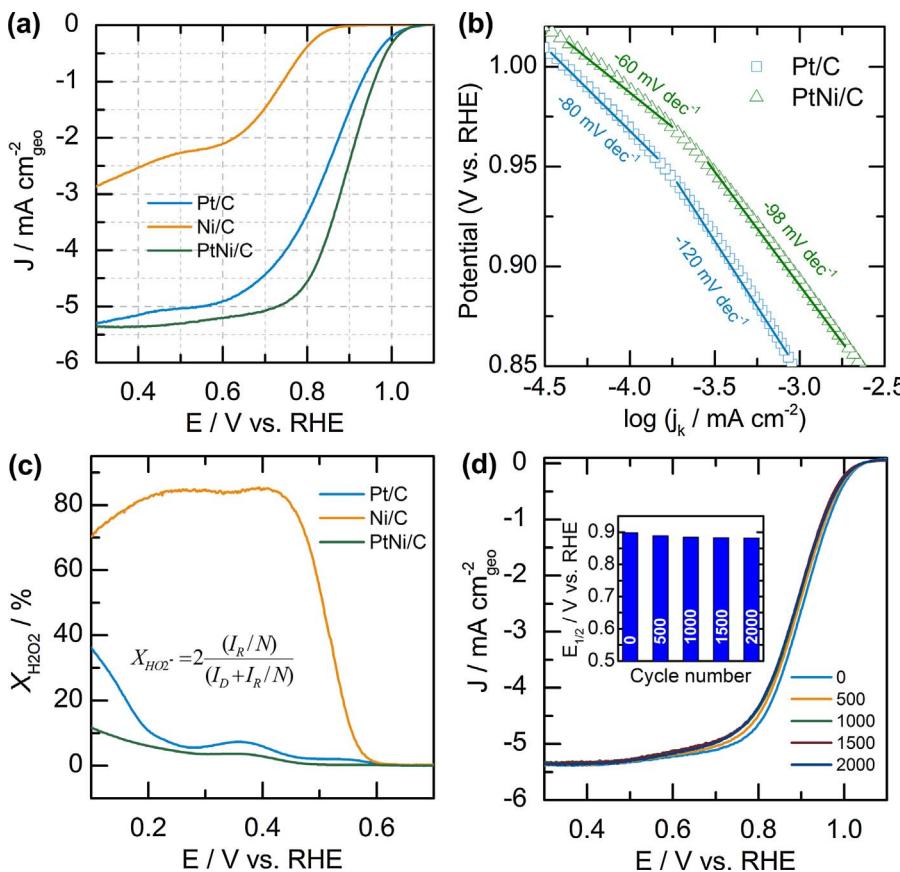


Fig. 3. ORR polarization curves (a), ORR Tafel plots (b) extracted from the ORR polarization curves in panel a, fraction of H₂O₂ formed during ORR (c), and ORR polarization curves after different potential cycles in O₂-saturated 0.1 M KOH solution. Inset in panel c: calculation of H₂O₂ fraction, where I_R represents the ring current, I_D is the disk current and N is the collection efficiency.

total Pt ECSA of 25.8 m² g_{Pt}⁻¹, which appears much lower than the experimentally determined Pt ECSA (38.4 m² g_{Pt}⁻¹). These results indicate that the inner surface is still accessible, and the porous structure in the PtNi shell could also contribute to the total ECSA of Pt, which provides another piece of proof that PtNi hollow particle would feature open porous structures. Another notable feature of the CV curves on PtNi/C is that the reduction current is dramatically boosted at the potential close to the cathodic vertex, which is stemming from the hydrogen evolution reaction (HER). In contrast, the hydrogen evolution process is not efficiently catalyzed on the reference Pt/C at the similar potential region. These results indicate that PtNi/C would be intrinsically more active towards hydrogen evolution process than the reference Pt/C, which is consistent with some recent reports [31,32].

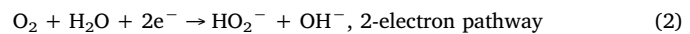
3.2. Oxygen reduction reaction

The electrocatalytic performance of PtNi/C for ORR was firstly investigated by using the rotating disk electrode (RDE) technique. Fig. 3a compares the ORR polarization curves in 0.1 M KOH of PtNi/C with those of Pt/C and Ni/C. Firstly, it can be observed that Ni/C exhibits rather poor activity for ORR as evidenced by the less developed diffusion limiting current plateau. In contrast, well defined diffusion limiting current plateaus can be observed on PtNi/C and Pt/C. To quantitatively compare the difference in activity, the specific activity (SA) was determined by normalizing the mass-transport corrected kinetic current to the ECSA of Pt, and compared at 0.9 V as a standard metric for ORR activity assessment. The SA of the PtNi/C is 0.56 mA cm_{Pt}⁻², which is 3 times that of the Pt/C (0.18 mA cm_{Pt}⁻²). This result is in line with Chattot et al.'s report that hollow structured PtNi (after acid leaching) could exhibit superior activity towards ORR in alkaline electrolyte compared to the reference Pt/C [25], again confirming that incorporation of Ni can not only accelerate the ORR kinetics on Pt in acidic electrolyte as well-documented in literature, but also improve the

Pt activity in an alkaline electrolyte.

We also conducted Tafel analysis to understand the difference in catalytic activity between PtNi/C and Pt/C by comparing their Tafel slopes, which indicate the overpotential that is needed to achieve a 10-fold increase in the current density. As shown in Fig. 3b, in the relatively low potential region (i.e., 0.90–0.95 V), the Tafel slope is around -120 mV dec⁻¹ on Pt/C, which is consistent with the intrinsic Tafel slope on clean Pt surfaces [33], indicating that the rate-determining step is the first charge transfer step process [34]. However, in the higher potential region (> 0.95 V), the Tafel slope quickly increases to -80 mV dec⁻¹, and the deviation from the -120 mV dec⁻¹ is ascribed to the formation of surface Pt oxide [33,35], and on this Pt/PtO surface, the rate determining step is believed to be a pseudo 2-electron procedure [36]. The Tafel plots on PtNi/C displays a similar two-state linear region at low and high potentials respectively. Interestingly, we found that PtNi/C always exhibits smaller Tafel slopes at both high (-60 mV dec⁻¹) and low (-98 mV dec⁻¹) electrode potentials than the reference Pt/C catalyst. The smaller Tafel slopes indicate that higher current density can be achieved on the PtNi/C at lower overpotential relative to the reference Pt/C, again verifying that PtNi/C catalyst is more efficient to accelerate ORR than the Pt/C catalyst [36,37].

ORR could take place either through the 4-electron pathway to produce water or 2-electron pathway to produce hydrogen peroxide species, i.e., HO₂⁻ in alkaline electrolyte:



For fuel cell or metal-air battery applications, the 4-electron pathway is highly preferred. Herein, to determine the ORR selectivity on the PtNi/C and the reference Pt/C and Ni/C catalysts, the rotating ring disk electrode (RRDE) technique has been employed, where glassy

carbon electrode was used as working electrode for catalyst coating, while an additional Pt ring electrode was used to collect and monitor the intermediate HO_2^- species during the ORR process (detail can be found in the Supporting Information). As shown in Fig. 3c, the mole fraction of HO_2^- formation during ORR is less than 10% ($E > 0.2$ V) on PtNi/C and Pt/C, indicating a predominant 4-electron pathway on both catalysts. In contrast, Ni/C would catalyze ORR mainly through the 2-electron pathway to produce HO_2^- species ($X_{\text{HO}_2^-} = 85\%$) over a wide potential range (Fig. S3). The durability of the PtNi/C catalyst was also evaluated by potential cycling between 0.6 and 1.0 V for 2000 cycles. As shown in Fig. 3d, the polarization curves were negatively shifted by 10 mV after 500 cycles, 15 mV after 1000 cycles and then stabilized up to 2000 cycles, indicating a fairly good stability performance PtNi/C towards ORR. It is noteworthy that after the stability test, the PtNi/C catalyst still exhibits a much higher $E_{1/2}$ (0.884 V) than the fresh Pt/C catalyst (0.845 V), demonstrating the great advantage of PtNi/C as a precious-metal-saving electrocatalyst.

3.3. Oxygen evolution reaction

The OER performance of the PtNi/C and the reference Pt/C and Ni/C catalysts were evaluated in 0.1 M KOH electrolyte, and the PtNi/C was also found highly active for OER in alkaline electrolyte (Fig. 4). As shown in Fig. 4a, this bimetallic catalyst requires an overpotential of only 350 mV to reach a current density of 10 mA cm^{-2} , which is lower than that of the reported state-of-the-art OER catalyst as IrO₂/C (360–370 mV) under similar conditions [5,11]. Meanwhile, the reference Ni/C is also highly active towards OER with an overpotential of 385 mV, while in contrast, the Pt/C fails to reach such current density due to the formation of the inactive surface oxide species [38,39]. To better compare the intrinsic activity of these catalysts for OER, the turnover frequency (TOF), which is defined as the number of catalytic

cycles executed per unit time on per active site, is calculated based on the following equation [40]:

$$\text{TOF} = \frac{\text{mol } \text{O}_2/\text{s}}{(\text{mol active sites})} = \frac{\text{OER current}/4F}{(\text{mol active sites})} \quad (3)$$

where F is the Faraday constant (96485.3 C/mol). For PtNi/C and Ni/C, the number of active sites was estimated by integrating the redox wave at around 1.4 V (Fig. S4), as detailed in the Supporting Information. In order to minimize the current density contribution from the carbon oxidation process at high potential region as shown in Fig. S5, the net OER current density which is determined by subtracting the oxidation current contribution from the carbon support, is employed to calculate the TOF values. It turns out that the PtNi/C exhibits a TOF value of 3.60 s^{-1} at an overpotential of 0.35 V, which is 4 and 93 times higher than those on Ni/C (0.86 s^{-1}) and Pt/C (0.04 s^{-1}), respectively, demonstrating that PtNi/C catalyst is intrinsically much more active towards OER than those monometallic counterparts.

Moreover, it is also found that the Tafel slope of PtNi/C is 60 mV dec^{-1} , which is significantly smaller than that of the reference Pt/C (290 mV dec^{-1}) and Ni/C (92 mV dec^{-1}) as shown in Fig. 4b, again demonstrating its superior OER activity, which might arise from the synergistic effect between the high intrinsic activity of Ni entities and excellent electronic conductivity of Pt phase within the bimetallic PtNi alloyed nanoparticles. This is consistent with the findings reported by Boettcher et al., that only the active sites (metal oxyhydroxides) close to the electronically conductive substrate (e.g., Pt, Au) are active towards OER [7,8]. Moreover, the electrochemical impedance spectroscopy (EIS) was employed to explore the electrode kinetics during OER processes, we resort to the application of a Randles-type model as the equivalent circuit. To account for the non-homogeneities of the electrode, we adapted the convention to replace capacitor elements by constant phase elements (CPE) [41]. CPE is defined by [42]:

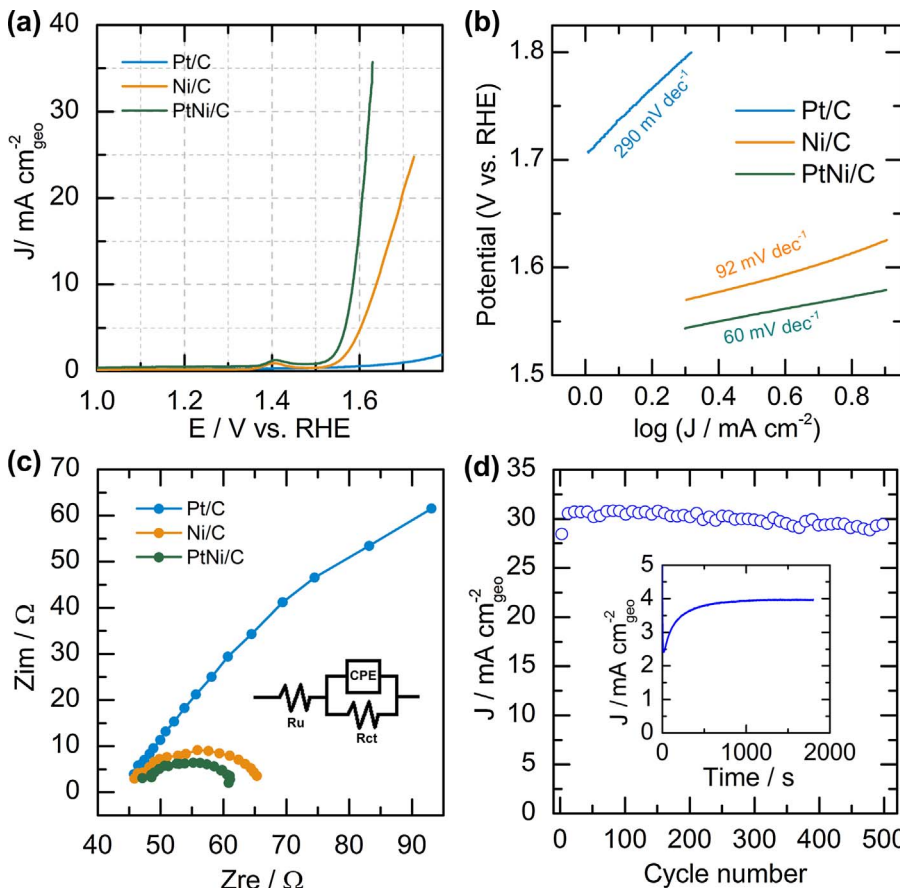


Fig. 4. OER polarization curves (a) and Tafel plots (b) of catalysts in O_2 -saturated 0.1 M KOH solution (pH=13). (c) EIS Nyquist plots of catalysts at 1.6 V vs. RHE, and the inset shows the equivalent circuit model, where CPE standing for the constant phase element, Ru and Rct are the solution resistance and charge transfer resistance, respectively. (d) Stability tests using repetitive CV and chronoamperometry modes.

$$Z_{CPE} = T_{CPE} (j\omega)^{-n} \quad (4)$$

where Z_{CPE} is the impedance of the CPE, T_{CPE} and n are frequency independent constants; ω is the angular frequency. The exponent n is the correction factor related to the roughness of an electrode, with value ranging from 0 to 1. $n = 1$ indicates that CPE is an ideal capacitor [43]. As illustrated in Fig. 4c, the Nyquist plots of both bimetallic PtNi/C and Ni/C feature a depressed semi-circle shape. The details for fitting the EIS data for Pt/C, Ni/C and PtNi/C are illustrated in Figs. S6, S7 and S8, respectively. The smaller diameter of the semi-circle PtNi/C verifies that the PtNi/C would possess lower charge transfer resistance $R_{CT}(4.2 \Omega \times \text{cm}^2)$ and also enhanced OER kinetics relative to the reference Pt/C ($66.5 \Omega \text{cm}^2$) and Ni/C ($5.5 \Omega \text{cm}^2$) [41,44,45], as listed in Table S3.

The electrochemical stability of the PtNi/C catalyst was evaluated by using two techniques, *i.e.*, dynamic repetitive CV cycling and static chronoamperometry (CA). It can be noticed that PtNi/C is a rather robust electrocatalyst for OER regardless of the testing modes, as reflected by the negligible current loss after the stability tests (Fig. 4d). This result is consistent with the report of Dubau et al., that the hollow structured PtNi/C could exhibit excellent electrochemical stability, showing little morphology change or particle migration/aggregation after the ORR accelerated durability test (reaction temperature $< 80^\circ \text{C}$) [46,47]. They suggest that the large contact surface area of the hollow PtNi with carbon support could contribute to its excellent electrochemical stability [47]. Although the significant activity loss can also be observed on PtNi/C under the practical PEMFC operation conditions (80°C) due to the dissolution of Ni species and/or structure collapse, the degraded PtNi/C is still intrinsically more active towards ORR than the fresh Pt/C catalyst [46,47].

In the present work, in order to track the structural change of PtNi/C sample after the above electrochemical stability (dynamic mode) measurements, we firstly made attempt to probe the change in the surface oxidation state of Pt and Ni using XPS (Fig. S9). The proportion of the metallic state Pt (Pt^0) has increased from 9.6% to 17.8% after the electrochemistry measurement, indicating that the surface oxidized Pt has been partially reduced. At the same time, we found that a shoulder peak appearing at 78.2 eV, which is absent in the XPS of the as-prepared PtNi/C. This peak ($\text{Pt } 4f_{5/2}$) can be attributed to the surface Pt that has strong interaction with fluorine species, which comes from the Nafion binding agent during the WE preparation. Unfortunately, we also found that the presence of fluorine species imposed severe disturbance on determining the oxidation state of Ni by featuring strong Auger peaks (F KLL) in the binding energy region of 820–900 eV, which are overlapped with the Ni 2p peaks. Attempts were then made to conduct the peak deconvolution, and the Ni 2p signal can still be resolved with the Ni 2p_{3/2} and 2p_{1/2} peaks centering at 853.5 and 870.8 eV, respectively. However, we have to admit that the complexity of Ni 2p peaks in combination of the F KLL signals has hindered our attempt to rationally determine the proportions of Ni species in metallic and/or oxidized states. Interestingly, we also found that, after the electrochemistry measurement, the surface atomic Ni/Pt ratio has increased from 0.25 to 0.35, indicating that the Ni species has the tendency to segregate to the surface during the electrochemistry measurement. Since the OER performance is relatively stable until up to 500 cycles, we assume that the surface segregation would likely occur during the electrochemistry pretreatment stage. After carefully checking the CV curves during the pretreatment (Fig. S10), we found that the major change in the surface state would take place in the first 15 cycles, where we can clearly see the evolution of Ni(II)/Ni(III) oxidation peak with increasing the cycle numbers. Later on, the oxidation peak is insensitive to the cycle numbers and reaches a relatively stable state. These results indicate that: 1) The PtNi/C sample has experienced a surface structural change during the electrochemical measurement, resulting partial segregation of Ni species to the particle surfaces; 2) The surface structural change especially the surface segregation of Ni

species likely took place during the electrochemical pretreatment stage, as evidenced by the phenomenon that the redox wave of Ni species has gradually strengthened during the first 15 cycles and then settled off (Fig. S10). Based on these results we would also suggest that for better probing the change of surface composition and chemical state of Pt and Ni using XPS during the electrochemical measurements in future works, it would become necessary to avoid using the disturbing species like Nafion in the current work.

Moreover, we have tracked the structural change of the PtNi/C after electrochemical measurement using TEM, STEM and EDS techniques. The TEM images display that after the electrochemical stability test, the PtNi particles still feature the hollow structure (Fig. S11). It can also be seen that the particles are well separated with each other without any severe particle aggregation or oriented attachment. The statistics indicate that the average PtNi particle size is around 15.4 nm, which is slightly larger than that of the as-prepared sample (15.0 nm), while the shell thickness remains constant after the electrochemical measurement. EDS elemental mapping was also used to probe the element distribution of a representative PtNi hollow particle after the electrochemical test, as shown in Fig. S12, the shadow in the interior of the particle implies the hollow structure of the PtNi particle, again verifying that the hollow structure is well maintained after the electrochemical measurement. At the same time, we also found that the Ni species distributed all over the shell even at the outer surface of the particle, which is different from the fresh PtNi particle on which the surface is dominated by the Pt species. This result is in line with the XPS analysis result, that the Ni species would segregate to the particle surface after the electrochemical test. The EDS elemental analysis confirms that the atomic Pt:Ni:C ratio is roughly comparable to that of the fresh PtNi/C sample (Fig. S13), which again verifies that PtNi/C sample is rather robust during the electrochemical measurement.

Based on the above results, it can be concluded that PtNi/C catalyst is an efficient electrocatalyst with both excellent activity and stability, and these results would provide the basis for practical applications of PtNi/C as the bifunctional electrocatalyst for metal-air batteries or URFCs applications. Table 1 clearly shows, based on comparison of the total overpotential of ORR and OER, that the present hollow structured PtNi/C catalyst is superior to those of the representative bifunctional precious metal based and precious metal free electrocatalysts documented in literature. PtNi/C appears to be the most efficient bifunctional electrocatalyst towards ORR and OER among the listed catalytic systems tested under similar measurement conditions (0.1 M KOH), exhibiting to date the lowest total overpotential value (0.69 V) for ORR and OER. To be noted, PtNi/C catalyst even outperforms some samples tested in 1.0 M KOH electrolyte, *e.g.*, PtCo with a total overpotential of 0.75 V [48] and Co₃O₄/N-graphene with a total overpotential of 0.71 V [49].

3.4. Origin of the superior catalytic activity of PtNi/C

The enhanced activity of PtNi/C towards ORR relative to Pt/C is not surprising because of the well-known down-shift of the Pt d-band center energy after alloying Pt with base metals, which would weaken the bonding strength between Pt and oxygenated species and result in an accelerated ORR kinetics [32,53–56]. Moreover, most recently Maillard et al. have demonstrated both experimentally and theoretically that, besides the conventional strain/ligand effect introduced by alloying Pt with Ni, the presence of structural defects (*e.g.*, grain boundaries, atomic vacancies) on the hollow structured PtNi/C sample after acid leaching treatment would also contribute to the dramatically enhanced ORR kinetics of PtNi/C relative to that of the reference Pt/C catalyst [46,57,58]. Regarding the OER, Ni species has long been recognized as an active phase for this reaction, which is also verified herein by the fairly high activity of Ni/C. However, it is intriguing to observe that PtNi/C could exhibit excellent performance towards OER, and this is nontrivial considering that Pt itself has poor activity and after the acid

Table 1

Comparison of the total overpotentials towards ORR and OER.

Sample	Electrolyte	$\eta_{\text{ORR}}/\text{V}^{\text{a}}$	$\eta_{\text{OER}}/\text{V}^{\text{b}}$	$\eta_{\text{total}}/\text{V}$	Year	Reference
MnO _x	0.1 M KOH	0.50	0.54	1.04	2010	[50]
Ru/C	0.1 M KOH	0.62	0.39	1.01	2010	[50]
Co ₃ O ₄ /graphene	1.0 M KOH	0.40	0.31	0.71	2011	[49]
Pt/CaMnO ₃	0.1 M KOH	0.44	0.57	1.01	2014	[51]
Pt/C-oxide composite	0.1 M KOH	0.42	0.38	0.80	2014	[52]
Ir/C	0.1 M KOH	0.50	0.37	0.87	2015	[11]
NiFe-LDH	0.1 M KOH	0.94	0.32	1.27	2016	[5]
Fe-N-C	0.1 M KOH	0.43	0.51	0.94	2016	[5]
NiFe-LDH + Fe-N-C (1:3)	0.1 M KOH	0.44	0.31	0.75	2016	[5]
Pt/C	0.1 M KOH	0.37	0.67	1.04	2016	[5]
PtCo	1.0 M KOH	0.36	0.38	0.76	2016	[48]
3D NCNT array	0.1 M KOH	0.42	0.42	0.84	2017	[37]
P,N-doped graphene	0.1 M KOH	0.38	0.32	0.71	2017	[6]
Pt/C + Ir/C	0.1 M KOH	0.40	0.35	0.75	2017	[6]
PtNi/C	0.1 M KOH	0.34	0.35	0.69 ± 0.01	2017	This work

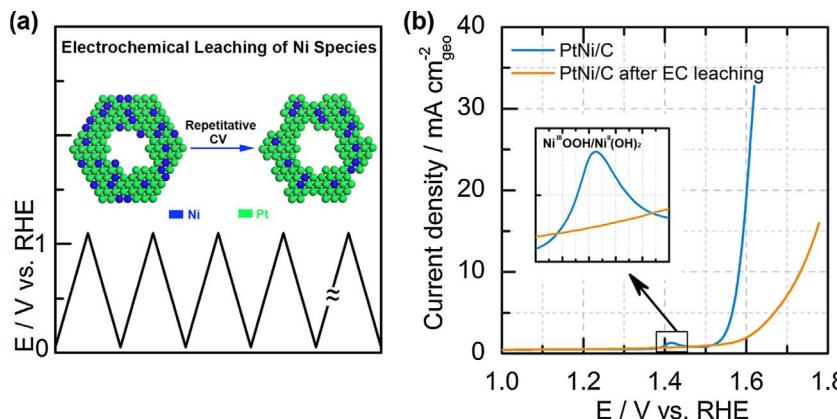
^a Defined as the difference between half-wave potential and the standard equilibrium potential of ORR.^b Defined as the difference between potential@10 mA cm⁻² and the standard equilibrium potential of OER.

Fig. 5. (a) Illustration of electrochemical leaching of Ni out of the PtNi/C sample using repetitive CV cycling in 0.1M HClO₄; (b) OER polarization curves of PtNi/C before and after electrochemical (EC) leaching treatment. The inset shows that no Ni species can be identified after the EC leaching pretreatment.

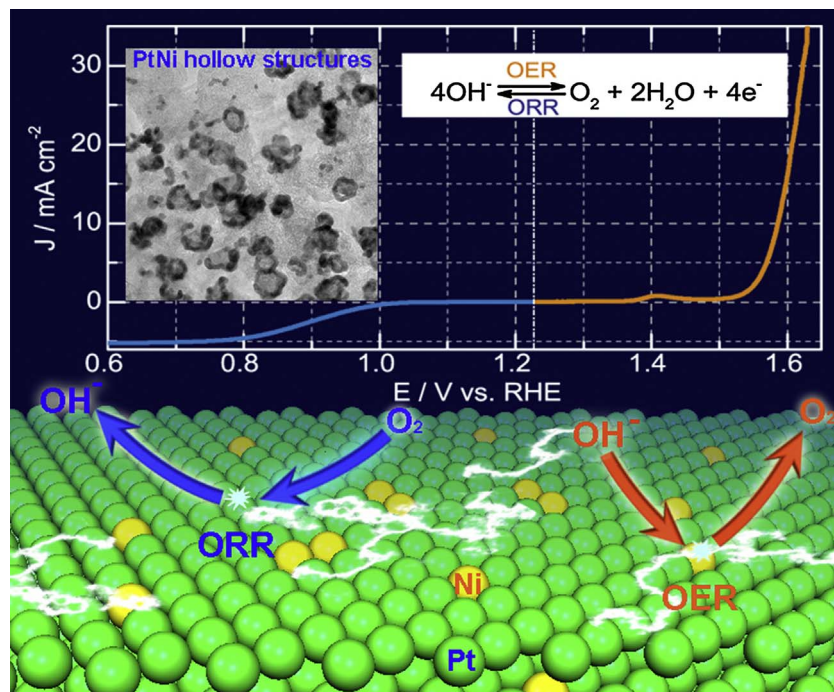


Fig. 6. Illustration of bifunctionality of PtNi/C towards ORR and OER. The Pt phase is shown in green, while the embedded Ni species is shown in yellow. (For interpretation of the references to colour in this figure legend, the reader is referred to the web version of this article).

leaching treatment the majority of the Ni species in PtNi/C has been removed as verified by the ICP and EDS analyses. By carefully inspecting the OER polarization curves, a minor peak centered at 1.4 V can be observed on PtNi/C and Ni/C samples. The peak is usually assigned to the oxidation of Ni(OH)_2 to NiOOH [40,59], and can thus be used as an indicator of the surface Ni species. The ICP analysis of the PtNi/C confirms the low Ni content after the acid leaching pretreatment. However, the minor peak on PtNi/C suggests that a certain amount of Ni has directly exposed to surfaces. To gain more insight into the role of the Ni in PtNi/C towards OER, an additional electrochemical leaching treatment to the as-prepared PtNi/C was performed in 0.1 M HClO_4 solution (Fig. 5a). Firstly, we found that the oxidation peak featuring surface Ni species is entirely vanished (Fig. 5b); Secondly, PtNi/C exhibited a dramatic drop in activity with overpotential increasing from 350 to 510 mV, while at the same time it is still much more active than the reference Pt/C. Based on these results, we can suggest that: i) The residual small amount of Ni on the surface of PtNi hollow nanoparticles plays a major role in catalyzing OER; ii) The underlying Ni species in a PtNi nanoparticle could help facilitate OER on Pt probably by retarding the formation of non-active Pt oxide thorough modifying its surface electronic structures (i.e., lowered d-band center).

As discussed above, the PtNi/C catalyst exhibits excellent performance towards both ORR and OER processes, which is achieved by properly integrating the active phases towards ORR and OER into a single catalyst through a facile solution-based synthetic method. The presence of the non-active phase (e.g., Ni towards ORR, Pt towards OER) hasn't sacrificed the activity of active phases, but acts as a structural promotor. For instance, the presence of Ni has caused lattice contraction of Pt (also lowered d-band center energies of Pt) and accelerated ORR on Pt, while the presence of Pt substrate could facilitate the electron transfer processes within the electrode material and therefore promote the OER on their embedded Ni species, as illustrated in Fig. 6. Compared to other state-of-the-art mixture/composites bifunctional electrocatalysts, the PtNi/C catalyst exhibits its superiority through the following aspects: 1) the record low total overpotential towards ORR and OER can be achieved on the PtNi/C, and the catalytic performance can be stabilized over the long-term operation; 2) the ORR or OER performance is not sacrificed in presence of the non-active phase, that is, it becomes unnecessary to maintain good performance of a single ORR/OER catalyst by increasing the loading of the precious metal materials [15,16]; 3) no tedious and/or high-temperature synthetic methodology has been involved, making the current method easy to scale-up; 4) the undesirable 2-electron ORR pathway is not triggered on PtNi/C, and this is different from those composite bifunctional electrocatalysts where the OER active phase would catalyze the ORR through the 2-electron pathway to produce hydrogen peroxide species [52]. These findings make us tend to believe the hollow structured PtNi/C catalyst could hold the potential to be a new benchmark bifunctional oxygen electrocatalyst.

4. Conclusion

In conclusion, we present herein the synthesis of hollow porous structured PtNi/C which can be used as a highly active and robust bifunctional electrocatalyst for ORR and OER. The catalytic performance of PtNi/C significantly outperforms the reference monometallic Pt/C or Ni/C, representing one of the most active catalytic system with a record low total overpotential towards ORR and OER. It is also found that the small amount of residual Ni in PtNi/C after acid leaching plays an essential role in controlling its catalytic properties by altering the crystalline structures of Pt (lattice contraction). These results demonstrate a new avenue to constructing highly efficient precious metal saving electrocatalysts, namely by properly integrating different metal components with desirable catalytic properties into one single nanostructure, and may have important impact on the design and synthesis of high-performing nanostructures for other technological applications.

Acknowledgements

The authors would like to express their appreciation to Prof. Bastian J.M. Etzold for his strong support in carrying out the research. We would greatly thank Mr. Michael George for his kind help on ICP, XRD and N_2 -sorption analyses. Mr. Karl Kopp is greatly acknowledged for his help on the XPS measurement and data analysis. We acknowledge AkzoNobel for providing the Ketjenblack materials.

Appendix A. Supplementary data

Supplementary data associated with this article can be found, in the online version, at <http://dx.doi.org/10.1016/j.apcatb.2017.09.066>.

References

- Y.F. Wang, D.Y.C. Leung, J. Xuan, H.Z. Wang, A review on unitized regenerative fuel cell technologies, part B: unitized regenerative alkaline fuel cell, solid oxide fuel cell, and microfluidic fuel cell, *Renew. Sust. Energ. Rev.* 75 (2017) 775–795.
- J.T. Zhang, Z.H. Zhao, Z.H. Xia, L.M. Dai, A metal-free bifunctional electrocatalyst for oxygen reduction and oxygen evolution reactions, *Nat. Nanotechnol.* 10 (2015) 444–452.
- G. Fu, Z. Cui, Y. Chen, L. Xu, Y. Tang, J.B. Goodenough, Hierarchically mesoporous nickel-iron nitride as a cost-efficient and highly durable electrocatalyst for Zn-air battery, *Nano Energy* 39 (2017) 77–85.
- M. Tahir, L. Pan, F. Idrees, X. Zhang, L. Wang, J.-J. Zou, Z.L. Wang, Electrocatalytic oxygen evolution reaction for energy conversion and storage: a comprehensive review, *Nano Energy* 37 (2017) 136–157.
- S. Dresp, F. Luo, R. Schmack, S. Kuhl, M. Gliech, P. Strasser, An efficient bifunctional two-component catalyst for oxygen reduction and oxygen evolution in reversible fuel cells, electrolyzers and rechargeable air electrodes, *Energy Environ. Sci.* 9 (2016) 2020–2024.
- G.-L. Chai, K. Qiu, M.-M. Titirici, C. Shang, Z. Guo, Active sites engineering leads to exceptional ORR and OER bifunctionality in P,N Co-doped graphene frameworks, *Energy Environ. Sci.* 10 (2017) 1186–1195.
- M.S. Burke, S. Zou, L.J. Enman, J.E. Kellon, C.A. Gabor, E. Pledger, S.W. Boettcher, Revised oxygen evolution reaction activity trends for first-Row transition-Metal (Oxy)hydroxides in alkaline media, *J. Phys. Chem. Lett.* 6 (2015) 3737–3742.
- S. Zou, M.S. Burke, M.G. Kast, J. Fan, N. Danilovic, S.W. Boettcher, Fe (Oxy)hydroxide oxygen evolution reaction electrocatalysis: intrinsic activity and the roles of electrical conductivity, substrate, and dissolution, *Chem. Mater.* 27 (2015) 8011–8020.
- G.R. Zhang, B.Q. Xu, Nano-size effect of Au catalyst for electrochemical reduction of oxygen in alkaline electrolyte, *Chin. J. Catal.* 34 (2013) 942–948.
- B.Y. Xia, Y. Yan, N. Li, H.B. Wu, X.W. Lou, X. Wang, A metal-organic framework-derived bifunctional oxygen electrocatalyst, *Nat. Energy* 1 (2016) 15006.
- Y. Zhao, K. Kamiya, K. Hashimoto, S. Nakanishi, Efficient bifunctional Fe/C/N electrocatalysts for oxygen reduction and evolution reaction, *J. Phys. Chem. C* 119 (2015) 2583–2588.
- Y. Wang, D.Y.C. Leung, J. Xuan, H. Wang, A review on unitized regenerative fuel cell technologies, part-A: unitized regenerative proton exchange membrane fuel cells, *Renew. Sustain. Energy Rev.* 65 (2016) 961–977.
- H. Liu, B. Yi, M. Hou, J. Wu, Z. Hou, H. Zhang, Composite electrode for unitized regenerative proton exchange membrane fuel cell with improved cycle life, *Electrochim. Solid-State Lett.* 7 (2004) A56–A59.
- H.-Y. Jung, S. Park, B.N. Popov, Electrochemical studies of an unsupported PtIr electrocatalyst as a bifunctional oxygen electrode in a unitized regenerative fuel cell, *J. Power Sources* 191 (2009) 357–361.
- S.-D. Yim, W.-Y. Lee, Y.-G. Yoon, Y.-J. Sohn, G.-G. Park, T.-H. Yang, C.-S. Kim, Optimization of bifunctional electrocatalyst for PEM unitized regenerative fuel cell, *Electrochim. Acta* 50 (2004) 713–718.
- S.-D. Yim, G.-G. Park, Y.-J. Sohn, W.-Y. Lee, Y.-G. Yoon, T.-H. Yang, S. Um, S.-P. Yu, C.-S. Kim, Optimization of PtIr electrocatalyst for PEM URFC, *Int. J. Hydrogen Energy* 30 (2005) 1345–1350.
- Y. Liu, D.C. Higgins, J. Wu, M. Fowler, Z. Chen, Cubic spinel cobalt oxide/multi-walled carbon nanotube composites as a efficient bifunctional electrocatalyst for oxygen reaction, *Electrochim. Commun.* 34 (2013) 125–129.
- Y.Y. Feng, G.R. Zhang, J.H. Ma, G. Liu, B.Q. Xu, Carbon-supported Pt⁺Ag nanostructures as cathode catalysts for oxygen reduction reaction, *Phys. Chem. Chem. Phys.* 13 (2011) 3863–3872.
- L. Jörissen, Bifunctional oxygen/air electrodes, *J. Power Sources* 155 (2006) 23–32.
- L.-L. Shen, G.-R. Zhang, S. Miao, J. Liu, B.-Q. Xu, Core-shell nanostructured Au@Ni_{1-x}Pt_x electrocatalysts with enhanced activity and durability for oxygen reduction reaction, *ACS Catal.* 6 (2016) 1680–1690.
- L. Dubau, T. Asset, R. Chattot, C. Bonnaud, V. Vanpeene, J. Nelayah, F. Maillard, Tuning the performance and the stability of porous hollow PtNi/C nanostructures for the oxygen reduction reaction, *ACS Catal.* 5 (2015) 5333–5341.
- L. Han, S. Dong, E. Wang, Transition-metal (Co Ni and Fe)-based electrocatalysts for the water oxidation reaction, *Adv. Mater.* (2016) 9266–9291.
- B. Zhang, X. Zheng, O. Voznyy, R. Comin, M. Bajdich, M. García-Melchor, L. Han, J. Xu, M. Liu, L. Zheng, F.P. García de Arquer, C.T. Dinh, F. Fan, M. Yuan,

E. Yassitepe, N. Chen, T. Regier, P. Liu, Y. Li, P. De Luna, A. Janmohamed, H.L. Xin, H. Yang, A. Vojvodic, E.H. Sargent, Homogeneously dispersed multimetal oxygen-evolving catalysts, *Science* 352 (2016) 333–337.

[24] P. He, X.-Y. Yu, X.W. Lou, Carbon-incorporated nickel–cobalt mixed metal phosphide nanoboxes with enhanced electrocatalytic activity for oxygen evolution, *Angew. Chem. Int. Ed.* (2017) 3897–3900.

[25] R. Chattot, T. Asset, J. Drnec, P. Bordet, J. Nelayah, L. Dubau, F. Maillard, Atomic-scale snapshots of the formation and growth of hollow PtNi/C nanocatalysts, *Nano Lett.* 17 (2017) 2447–2453.

[26] J. Gläsel, J. Diao, Z. Feng, M. Hilgart, T. Wolker, D.S. Su, B.J.M. Etzold, Mesoporous and graphitic carbide-derived carbons as selective and stable catalysts for the dehydrogenation reaction, *Chem. Mater.* 27 (2015) 5719–5725.

[27] L. Dubau, J. Nelayah, S. Moldovan, O. Ersen, P. Bordet, J. Drnec, T. Asset, R. Chattot, F. Maillard, Defects do catalysis: CO monolayer oxidation and oxygen reduction reaction on hollow PtNi/C nanoparticles, *ACS Catal.* 6 (2016) 4673–4684.

[28] B.Y. Xia, H.B. Wu, N. Li, X.W. Yan, X. Wang, One-Pot synthesis of Pt–Co alloy nanowire assemblies with tunable composition and enhanced electrocatalytic properties, *Angew. Chem. Int. Ed.* 54 (2015) 3797–3801.

[29] G.R. Zhang, J. Wu, B.Q. Xu, Syntheses of sub-30 nm Au@Pd concave nanocubes and Pt-on-(Au@Pd) trimetallic nanostructures as highly efficient catalysts for ethanol oxidation, *J. Phys. Chem. C* 116 (2012) 20839–20847.

[30] L. Ma, C. Wang, B.Y. Xia, K. Mao, J. He, X. Wu, Y. Xiong, X.W. Lou, Platinum multicubes prepared by Ni²⁺-Mediated shape evolution exhibit high electrocatalytic activity for oxygen reduction, *Angew. Chem. Int. Ed.* 54 (2015) 5666–5671.

[31] Z. Cao, Q. Chen, J. Zhang, H. Li, Y. Jiang, S. Shen, G. Fu, B. -a. Lu, Z. Xie, L. Zheng, Platinum–nickel alloy excavated nano-multipods with hexagonal close-packed structure and superior activity towards hydrogen evolution reaction, *Nat. Commun.* 8 (2017) 15131.

[32] C. Chen, Y.J. Kang, Z.Y. Huo, Z.W. Zhu, W.Y. Huang, H.L.L. Xin, J.D. Snyder, D.G. Li, J.A. Herron, M. Mavrikakis, M.F. Chi, K.L. More, Y.D. Li, N.M. Markovic, G.A. Somorjai, P.D. Yang, V.R. Stamenkovic, Highly crystalline multimetallic nanoframes with three-Dimensional electrocatalytic surfaces, *Science* 343 (2014) 1339–1343.

[33] N.P. Subramanian, T.A. Greszler, J. Zhang, W. Gu, R. Makharia, Pt-Oxide coverage-Dependent oxygen reduction reaction (ORR) kinetics, *J. Electrochem. Soc.* 159 (2012) B531–B540.

[34] N.M. Marković, H.A. Gasteiger, B.N. Grgur, P.N. Ross, Oxygen reduction reaction on Pt(111): effects of bromide, *J. Electroanal. Chem.* 467 (1999) 157–163.

[35] G.R. Zhang, M. Munoz, B.J. Etzold, Accelerating oxygen-reduction catalysts through preventing poisoning with non-reactive species by using hydrophobic ionic liquids, *Angew. Chem., Int. Ed.* 55 (2016) 2257–2261.

[36] C. Song, J. Zhang, Electrocatalytic oxygen reduction reaction, in: J. Zhang (Ed.), PEM Fuel Cell Electrocatalysts and Catalyst Layers: Fundamentals and Applications, Springer London, London, 2008, pp. 89–134.

[37] Z. Li, M. Shao, Q. Yang, Y. Tang, M. Wei, D.G. Evans, X. Duan, Directed synthesis of carbon nanotube arrays based on layered double hydroxides toward highly-efficient bifunctional oxygen electrocatalysis, *Nano Energy* 37 (2017) 98–107.

[38] T. Reier, M. Oezaslan, P. Strasser, Electrocatalytic oxygen evolution reaction (OER) on Ru, Ir, and Pt catalysts: a comparative study of nanoparticles and bulk materials, *ACS Catal.* 2 (2012) 1765–1772.

[39] T. Reier, H.N. Nong, D. Teschner, R. Schlägl, P. Strasser, Electrocatalytic oxygen evolution reaction in acidic environments – reaction mechanisms and catalysts, *Adv. Energy Mater.* (2016) 1601275.

[40] M.B. Stevens, L.J. Enman, A.S. Batchellor, M.R. Cosby, A.E. Vise, C.D.M. Trang, S.W. Boettcher, Measurement techniques for the study of thin film heterogeneous water oxidation electrocatalysts, *Chem. Mater.* 29 (2017) 120–140.

[41] A. Papaderakis, D. Tsiplakides, S. Balomenou, S. Sotiropoulos, Electrochemical impedance studies of IrO₂ catalysts for oxygen evolution, *J. Electroanal. Chem.* 757 (2015) 216–224.

[42] J.-B. Jorcin, M.E. Orazem, N. Pébère, B. Tribollet, CPE analysis by local electrochemical impedance spectroscopy, *Electrochim. Acta* 51 (2006) 1473–1479.

[43] Y. Jin, M. Jia, M. Zhang, Q. Wen, Preparation of stable aqueous dispersion of graphene nanosheets and their electrochemical capacitive properties, *Appl. Surf. Sci.* 264 (2013) 787–793.

[44] Y. Meng, W. Song, H. Huang, Z. Ren, S.-Y. Chen, S.L. Suib, Structure–Property relationship of bifunctional MnO₂ nanostructures: highly efficient, ultra-Stable electrochemical water oxidation and oxygen reduction reaction catalysts identified in alkaline media, *J. Am. Chem. Soc.* 136 (2014) 11452–11464.

[45] M.Q. Yu, Y.H. Li, S. Yang, P.F. Liu, L.F. Pan, L. Zhang, H.G. Yang, Mn₃O₄ nano-octahedrons on Ni foam as an efficient three-dimensional oxygen evolution electrocatalyst, *J. Mater. Chem. A* 3 (2015) 14101–14104.

[46] L. Dubau, J. Nelayah, T. Asset, R. Chattot, F. Maillard, Implementing structural disorder as a promising direction for improving the stability of PtNi/C nanoparticles, *ACS Catal.* 7 (2017) 3072–3081.

[47] L. Dubau, M. Lopez-Haro, J. Durst, F. Maillard, Atomic-scale restructuring of hollow PtNi/C electrocatalysts during accelerated stress tests, *Catal. Today* 262 (2016) 146–154.

[48] S. Hu, G. Goenaga, C. Melton, T.A. Zawodzinski, D. Mukherjee, PtCo/CoOx nanocomposites: bifunctional electrocatalysts for oxygen reduction and evolution reactions synthesized via tandem laser ablation synthesis in solution-galvanic replacement reactions, *Appl. Catal. B: Environ.* 182 (2016) 286–296.

[49] Y. Liang, Y. Li, H. Wang, J. Zhou, J. Wang, T. Regier, H. Dai, Co₃O₄ nanocrystals on graphene as a synergistic catalyst for oxygen reduction reaction, *Nat. Mater.* 10 (2011) 780–786.

[50] Y. Gorlin, T.F. Jaramillo, A bifunctional nonprecious metal catalyst for oxygen reduction and water oxidation, *J. Am. Chem. Soc.* 132 (2010) 13612–13614.

[51] X. Han, F. Cheng, T. Zhang, J. Yang, Y. Hu, J. Chen, Hydrogenated uniform Pt clusters supported on porous CaMnO₃ as a bifunctional electrocatalyst for enhanced oxygen reduction and evolution, *Adv. Mater.* 26 (2014) 2047–2051.

[52] Y. Zhu, C. Su, X. Xu, W. Zhou, R. Ran, Z. Shao, A. Universal, Facile way for the development of superior bifunctional electrocatalysts for oxygen reduction and evolution reactions utilizing the synergistic effect, *Chem. – Eur. J.* 20 (2014) 15533–15542.

[53] F.H.B. Lima, J. Zhang, M.H. Shao, K. Sasaki, M.B. Vukmirovic, E.A. Ticianelli, R.R. Adzic, Catalytic activity-d-band center correlation for the O₂ reduction reaction on platinum in alkaline solutions, *J. Phys. Chem. C* 111 (2007) 404–410.

[54] M. García-Contreras, S. Fernández-Valverde, R. Basurto-Sánchez, Investigation of oxygen reduction in alkaline media on electrocatalysts prepared by the mechanical alloying of Pt, Co, and Ni, *J. Appl. Electrochem.* 45 (2015).

[55] G.R. Zhang, M. Munoz, B.J. Etzold, Boosting performance of low temperature fuel cell catalysts by subtle ionic liquid modification, *ACS Appl. Mater. Interfaces* 7 (2015) 3562–3570.

[56] G.R. Zhang, D. Zhao, Y.Y. Feng, B.S. Zhang, D.S. Su, G. Liu, B.Q. Xu, Catalytic pt-on-Au nanostructures: why Pt becomes more active on smaller Au particles, *ACS Nano* 6 (2012) 2226–2236.

[57] R. Chattot, T. Asset, P. Bordet, J. Drnec, L. Dubau, F. Maillard, Beyond strain and ligand effects microstrain-Induced enhancement of the oxygen reduction reaction kinetics on various PtNi/C nanostructures, *ACS Catal.* 7 (2017) 398–408.

[58] O. Le Bacq, A. Pasturel, R. Chattot, B. Previdello, J. Nelayah, T. Asset, L. Dubau, F. Maillard, Effect of atomic vacancies on the structure and the electrocatalytic activity of Pt-rich/C nanoparticles: a combined experimental and density functional theory study, *Chemcatchem* 9 (2017) 2324–2338.

[59] L. Wang, H. Chen, Q. Daniel, L. Duan, B. Philippe, Y. Yang, H. Rensmo, L. Sun, Promoting the water oxidation catalysis by synergistic interactions between Ni(OH)₂ and carbon nanotubes, *Adv. Energy Mater.* 6 (2016) 1600516.